Journal of Applied Geophysics 173 (2020) 103927

Contents lists available at ScienceDirect

Journal of Applied Geophysics

journal homepage: www.elsevier.com/locate/jappgeo

S-wave seismic imaging of near-surface sediments using tailored processing strategies

Thomas Burschil *, Hermann Buness

Leibniz Institute for Applied Geophysics, Stilleweg 2, 30655 Hannover, Germany

ARTICLE INFO

Article history:
Received 4 August 2019
Received in revised form 18 December 2019
Accepted 25 December 2019
Available online 26 December 2019

Keywords:
Near-surface structures
High-resolution
SH-wave
Horizontally-polarized shear wave
Overdeepened valley
Tannwald Basin

ABSTRACT

Reflection seismic imaging using horizontally-polarized S-waves (SH) can increase resolution and it could be cost-efficient compared to the common use of P-waves. However, since S-wave application often delivers varying data quality, appropriate processing schemes are required for particular imaging and interpretation purposes. In this paper, we present four tailored processing strategies that are applied to SH-wave data acquired in an overdeepened Quaternary basin in the Alpine foreland, the Tannwald Basin. The applied processing schemes consist of (1) processing using a short automatic gain control window that enhances structural details and highlights small-scale structures, (2) offset restriction indicating that relative small offsets are sufficient for adequate imaging, which offers reduced field operation costs, (3) coherency-enhancement that reveals large-scale structures for interpretation, and (4) adapted amplitude scaling that enables structural comparison of P-wave and S-wave seismic sections.

With respect to P-wave data measured on the same profile, we demonstrate the benefits of the S-wave seismic reflection method. P-waves offer robust imaging results, but S-waves double the resolution, better depict shallow reflections, and may image reflectors in areas where the P-wave struggles. At least for the Tannwald Basin, S-wave imaging is also more cost-efficient than P-wave imaging.

1. Introduction

Seismic reflection imaging is a well-established tool to determine subsurface boundaries of geological, hydrogeological, or other nature. Applying compressional waves (P-waves) is the common method, e.g. in exploration seismology, for deep targets up to several km. For environmental and engineering geophysics (Steeples and Miller, 1988), it provides images of shallow targets up to several 100 m in high resolution. However, some challenges occur during P-wave application on land that either inflate the acquisition costs or limit the structural resolution. Refracted and guided waves as well as surface waves and source-generated noise diminish the commonly-used part of seismic reflections in the seismograms (Steeples and Miller, 1998). Typically, the different propagation velocities of seismic waves separate the wavefield and allow discriminating different parts of a seismogram for shallow reflection imaging. Hunter et al. (1984) defined one of this parts as an "optimum window" for seismic reflection imaging. In this window, reflections do not interfere with P-wave first arrivals or surface wave ground-roll and can be used for reflection imaging without filtering these signals. Its utilization requires large source-receiver distances (offsets) relative to the depth of the reflectors. On the other hand, dense source and receiver spacings are mandatory to avoid spatial aliasing of the recorded wavefields. The combination of large offsets and dense spacing raises the acquisition costs for near-surface P-wave reflection seismic imaging. In addition, structural resolution is limited by the maximum usable frequency of the source, e.g. explosives or seismic vibrators that possess a maximum frequency range for excitation of the seismic wave (Buness, 2007). An extensive seismic processing can improve the structural resolution of near-surface data (Bradford et al., 2006; Burschil et al., 2018), but only in the mentioned limits of P-waves.

The usage of shear waves (S-waves) in the seismic reflection method (Pugin et al., 2013; Krawczyk et al., 2013) is a tool to overcome the limited resolution of P-waves and to decrease the seismic imaging costs. S-waves propagate slower than P-waves by nature so that they offer higher resolution at a similar frequency bandwidth range (Burschil et al., 2015). Due to the lower propagation velocity, the usable part of S-wave reflections occurs in the seismograms at smaller offsets compared to P-waves. They often show interference with high-amplitude surface waves, where the latter often hide the S-wave reflections due to their significantly stronger amplitudes. Unless the site characteristics involve a high-velocity top layer that suppresses the generation of interfering surface waves during acquisition (e.g. Inazaki, 2004; Polom et al., 2010), surface waves need to be removed during seismic processing workflow (e.g. Wadas et al., 2016).

* Corresponding author.
E-mail address: Thomas.Burschil@leibniz-liag.de (T. Burschil).

https://doi.org/10.1016/j.jappgeo.2019.103927

S-wave seismic reflection imaging has been applied to near-surface either in the horizontally-polarized S-wave domain (Inazaki, 2004; Polom et al., 2010) or in the vertically-polarized S-wave domain (Pugin et al., 2009). Several studies successfully investigated shallow targets of <30 m by structural interpretation of reflection patterns, e.g. of the bedrock topography (Polom et al., 2017), fractured environments in context to sinkhole formation (Wadas et al., 2017; Polom et al., 2018), or pathways for aquifer contamination (Malehmir et al., 2018). Furthermore, seismic velocity can be used for interpretation, e.g. a reduced interval velocity may indicate dissolved rock (Krawczyk et al., 2012; Tschache et al., 2018), or a change in interval velocities within layers may indicate different delta deposits (Winsemann et al., 2018). In addition, ground-engineering parameters, like the dynamic shear modulus, can be derived from the propagation velocity (e.g. Mavko et al., 2009; Uhlemann et al., 2016).

Data quality varies between the above-mentioned S-wave studies, even in the same study area (e.g. Carvalho et al., 2016). For all of these studies, one specifically adjusted seismic processing scheme was applied to process the data to an optimized seismic section. The aim of this paper is to highlight different processing strategies for horizontally-polarized S-wave imaging. The paper reflects our experience in S-wave seismic imaging and does not claim to be comprehensive. The geological target of investigation is an overdeepened Quaternary basin in the Rhine Glacier controlled Alpine foreland, i.e. the Tannwald Basin (TB) (Fig. 1), previously studied using P-wave reflection seismic method (Burschil et al., 2018).

2. Geological settings

The Alpine Orogeny caused the formation of the Molasse Basin in the northern Alpine foreland (Pfiffner, 1986). During the Pleistocene and the glaciations of the Alps, several ice advances of the Alpine Rhine Glacier moved over the Alpine Molasse Basin (Seguinot et al., 2018) and controlled the landscape evolution. Glacial erosion formed a system of overdeepened valleys and basins (Ellwanger et al., 2011). Glacial, lacustrine, and fluvial deposits sequentially filled these basins. Topographic highs remain in areas between the basins in the Rhine glacier affected area. Classification in terms of erosion and accumulation cycles determines three main formations (Fm.), based on the lithostratigraphy (from oldest to youngest): Dietmanns Fm., Illmensee Fm., and Hassenweiler Fm. Chronostratigraphically, these correspond to periods that comprise subsequent glaciation stages: Hosskirchian-Rissian, Rissian-Wurmian, and Wurmian-Present, respectively.

The studied area of the Tannwald Basin (TB) is located near the margin of the last glacial maximum (Fig. 1). The depth of the north-south-elongated basin varies between 80 m and 240 m. Burschil et al. (2018) interpreted the seismic facies on five seismic P-wave profiles, supported by a research borehole (locations in Fig. 1b). The seismic reflections image the substratum of the molasse units and reveal the sedimentary succession: glacial deposits of basal till, lacustrine deposits, and till sequences of the Dietmanns Fm. (Hosskirchian-Rissian stage), till and till sequences of the Illmensee Fm. (Rissian-Wurmian stage) as well as fluvial deposits of the outwash plain (Wurmian-Present stage). Thus, the TB forms an overdeepened Dietmanns basin and an area between Ilmensee basins, where no overdeepened erosion occurred during this stage.

3. Reflection seismic method

3.1. Field acquisition

Since 2014, Leibniz Institute of Applied Geophysics (LIAG) conducted several reflection seismic surveys in the TB. Data of two P-wave surveys using vertically-oriented sources and receivers constitute the base for the seismic interpretation (Burschil et al., 2018). In 2015, we recorded two S-wave profiles along previously measured

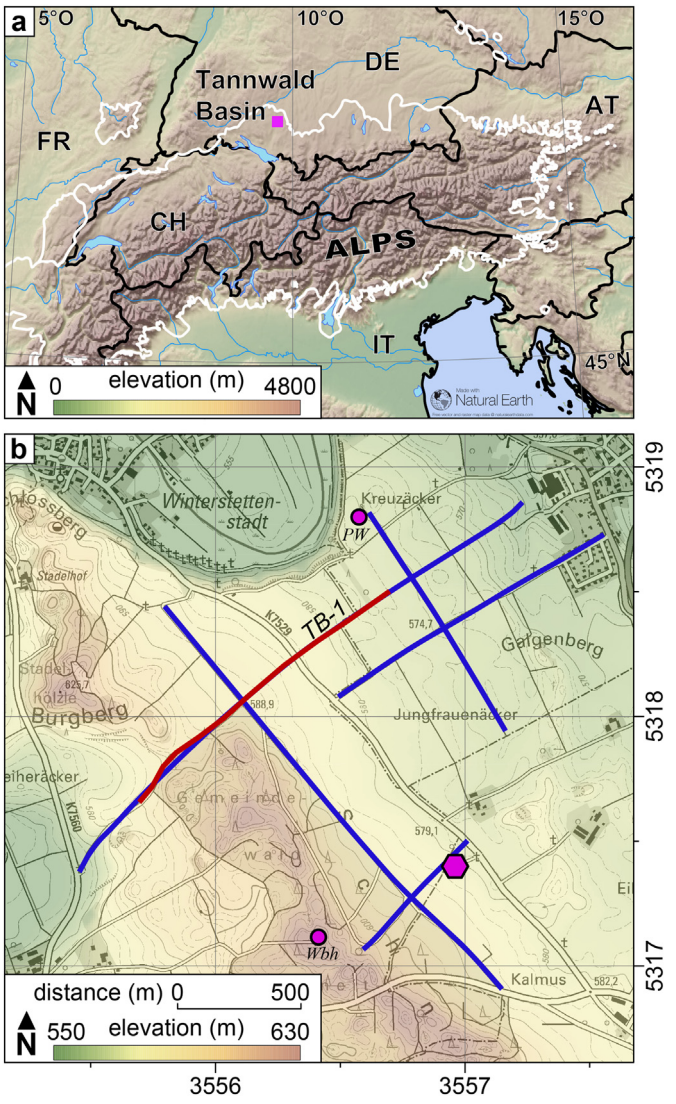

Fig. 1. Elevation map (a) of the European Alps showing the location of the Tannwald Basin in the Alpine foreland. The white line denotes the maximum ice extent during the last glacial maximum. The survey location map (b) shows elevation and seismic P-wave profiles in blue (Burschil et al., 2018) as well as the S-wave profile presented in this paper (red), the borehole Schneidermartin (magenta hexagon; described in Burschil et al., 2018), the water supply wells with pumping station *PW*, and the elevated water tank *Wbh* (magenta circles). The overview map was created using Natural Earth; Source of topographical map: © GeoBasis-DE / BKG 2019.

P-wave profiles. In our acquisition setup, both sources and receivers are oriented perpendicular to the profile direction to enable generation and analysis of horizontally polarized S-waves (SH-waves). The acquisition parameters for P-wave and S-wave surveys are summarized in Table 1. Weather conditions were sunny and calm during all surveys. For the S-wave survey, we acquired 2.1 km of profile in total, in five days of operation, including half a day of source tests. The crew consist of 4 members. In both P-wave surveys, we acquired 7.9 km of profile in total in 16 days of operation with 5 crew members.

In the following, we focus on profile TB-1 of the S-wave survey (Fig. 1b), because it contains various surface conditions (Fig. 2a). LIAG's horizontal hydraulic vibrator MHV4-S was used as seismic source and geophones mounted on two landstreamers of 120 m length each (1 m receiver spacing), recorded the earth response (Fig. 2a). The ground condition varied along the profile from asphalted road surface via a consolidated gravel path to a field path (Fig. 2b). At each shot location, we recorded four sweeps and changed the sweep polarization after two

Table 1
Acquisition details.

Acquisition parameter	S-wave survey	P-wave surveys
Source	Hydraulic Minivibrator MHV4S	Hydraulic Minivibrator HVP-30
Source point spacing	4 m	5 m
Vertical stack	4	2
Source signal	Linear sweep, 10–100 Hz, 10 s	Linear sweep, 20–200 Hz, 10 s
Receiver coupling	Landstreamer	Planted geophones
Receiver type	Sensor SM6-H, horizontal	Sensor SM6, vertical
Receiver spacing	1 m	2.5 m
No. of channels	240	360
Acquisition procedure	Split spread/roll along	
Recording unit	Geometrics Geode	
Sampling rate	2 ms	1 ms
Recording time	3 s	2 s
Vibroseis field correlation	On	
Field operation time for TB-1	2 days	5 days
Number of crew	4	5
Length of profile TB-1	1.33 km	2.4 km
Profile meters per day and person	162 m/d	96 m/d

excitations (++−). The shot gathers show reproducible signals at the same shot point (SP). We chose a source-receiver layout that enables a balanced updip-downdip layer detection sensitivity. During production, SPs were located at 4 m intervals in the first quarter of the 240 m-long spread (split-spread). After 60 m, both landstreamers were moved one quarter of the spread ahead (roll-along). At the SW end of the profile, shots were vibrated over the entire receiver spread plus 60 m end-on SPs. To prevent traffic obstruction while crossing the K7529 road with the landstreamers, we measured two individual profile sections: Both sections start at the road, operating away from the road. To close the coverage gap and to gain the same offset range as within the profile segments, end-on SPs on the opposite sides of the road allowed the fusion of the profiles. The operating and SP arrangement of the profile is shown for the first, two consecutive, and the last spreads in Fig. 2c.

The field data show low environmental noise (Fig. 3) and clear reflections in unprocessed shot gathers from shallow parts up to 0.7 s recording time (blue arrows in Fig. 3). Love surface waves with higher amplitudes occur in areas of unconsolidated ground surface (red arrows in Fig. 3), while they are not obvious in parts with asphalted or consolidated ground conditions (yellow arrows in Fig. 3). At a profile distance of 1420 m, the surface waves in the shot gathers show a significant variation that is not evident in the ground conditions, the landscape, or the geological map (green arrow in Fig. 3). The affected region is approximately 20 m wide. Seismic velocities of the surface waves (~500 m/s) and refracted waves (~700 m/s) are alike on both side of this zone (not shown), whereas the velocity of the direct wave is significantly lower (~250 m/s).

3.2. Seismic processing

For this comparison study of different processing strategies, we adapted an S-wave processing scheme that was used for various studies

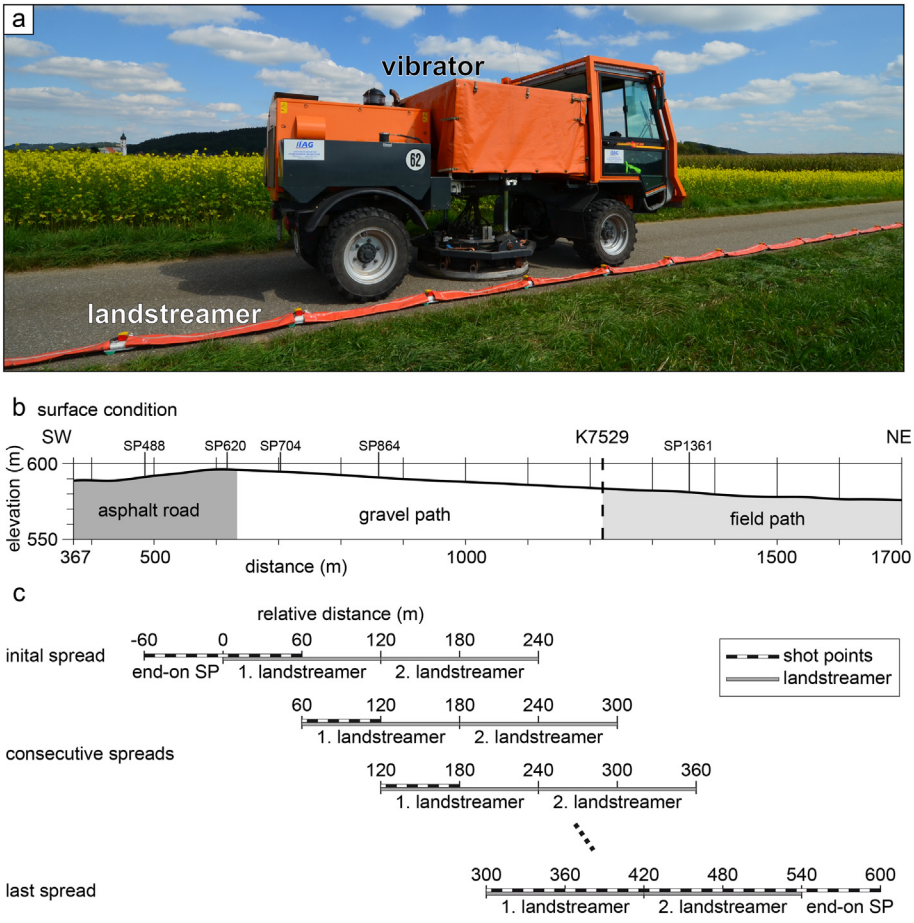

Fig. 2. LIAG vibrator MHV4-S and landstreamer during data acquisition (a), surface conditions along the S-wave section of profile TB-1 (b), and acquisition geometry (c). We applied a split-spread roll-along technique for acquisition (described in the text). The black-white bar denotes the positions of the source points (4 m intervals) and the gray bar denotes the positions of the two landstreamers (each 120 m length, 1 m receiver spacing) for the initial, two consecutive, and the last spreads. Photo: LIAG, T. Burschil.

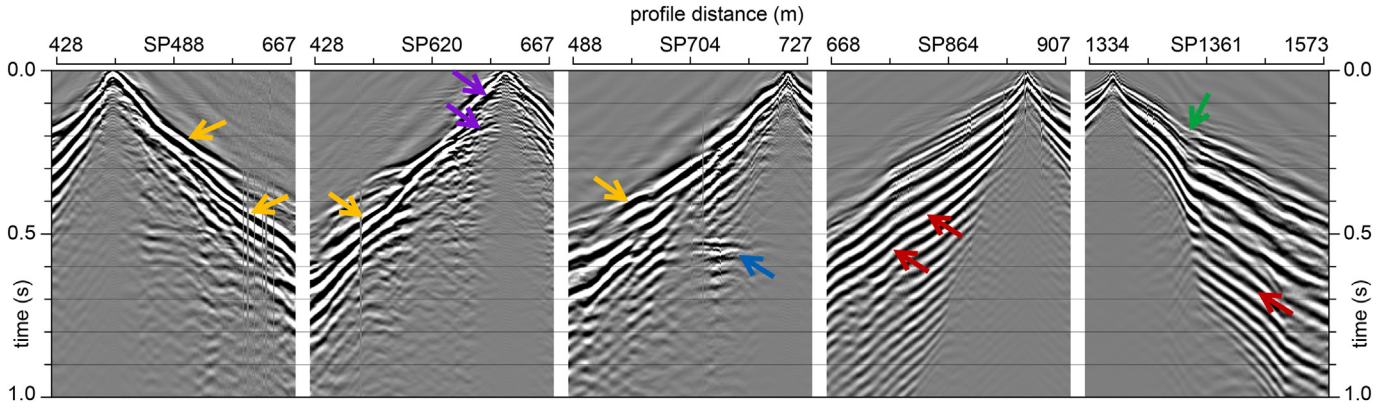

Fig. 3. SH-wave shot gather examples (pilot sweep vibroseis correlation applied) along profile TB-1 with trace normalization applied for imaging. The shallow and deep reflections are denoted by purple and blue arrows, resp. Note the difference of direct/refracted waves on the consolidated ground (yellow arrows) and the Love surface waves on the gravel and field path (red arrows). A change in near-surface conditions occurs along the field path (green arrow).

(Krawczyk et al., 2012; Wadas et al., 2016; Polom et al., 2018). Field data were processed using the Seisspace® software package. The major processing steps comprised signal enhancement (Fig. 4), normal move-out (NMO) correction with stacking velocities received by an iterative velocity analysis (Fig. 5), common midpoint (CMP) stacking, and poststack time migration. The application of different filters and the adaption of the processing parameters were the main adjustments to highlight different details in the final seismic section (Fig. 6; Table 2; see also Supplementary material).

All processing flows comprised adding geometry to the field data, vertical stacking, eliminating noisy traces, and static correction for the topography (Fig. 4a). After several tests with amplitude scaling, including true amplitude recovery, we decided to use automatic gain control (AGC) with different window lengths, which showed best results (Fig. 4b). Spectral whitening flattened the power spectrum range and increased resolution (Figs. 4c, e). It also reduced high-frequency, source-generated noise, which was undesirably amplified by AGC (green arrow in Fig. 4). A crucial step was the elimination of surface waves, tested by different approaches. Filtering in the f-k domain reduced the surface waves best (Fig. 4d). A selective application of the f-k-filter only to shot gathers, in which surface waves are present, generated post-stack artefacts at the edge of the region where we applied the filter. It resulted in less coherent reflectors in the stacked section.

Several iterations of interactive velocity analysis of the reflection hyperbolas in the CMP gathers were required to gain sufficiently accurate stacking velocities along the whole profile. Subsequently, we derived interval velocities in depth from stacking velocities by the smoothed gradient method (Sheriff and Geldart, 1995). The velocity distribution can be divided into two areas (black dashed line in Fig. 5): (1) an upper unit of 40 m thickness with a mean velocity of 517 m/s and a slightly increasing velocity gradient in depth (466 m/s at surface to 580 m/s at 30 m depth), and (2) a lower unit of 638 m/s with small variation (standard deviation of 25 m/s). However, small-scale, shallow velocity variations within the upper unit were not resolved in the stacking velocities. A tomography study of the S-wave first arrivals did not show a strongly varying near-surface velocity field either. Nonetheless, reflections exhibit deviations up to 10 ms from a hyperbolic shape in the shot gather (blue arrows in Fig. 4) as well as in the CMP gather, which we assign to near-surface velocity anomalies. Residual static corrections after NMO correction in a maximum shift range of ±5 ms reduced these effects without risking cycle shifts. 100% stretch mute applied during NMO correction muted the S-wave first arrivals. It includes a significant wider range for constructive wavelet stacking than is common for P-wave processing (e.g. 30–50%), as a result of the stronger hyperbola curvatures and velocity gradients at depth compared to P-waves.

After NMO correction and CMP stacking, processing comprised f-k-filtering (for one strategy only), finite difference (FD) time migration, data enhancement using a dip scan stack that reduces high-frequency, steep-dipping artefacts in the seismic section, and time-to-depth conversion using a smoothed version of the stacking velocity field.

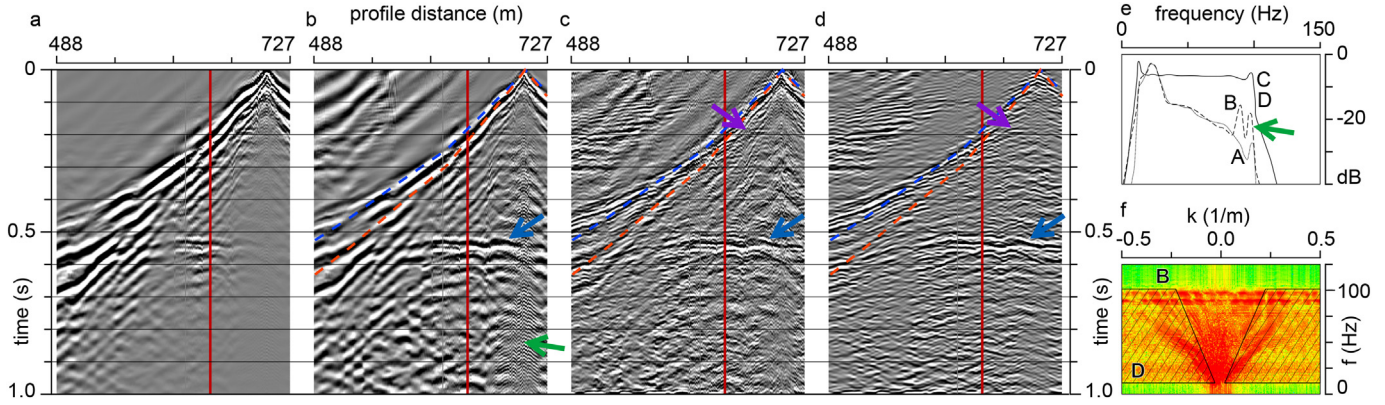

Fig. 4. Example shot gather SP704 demonstrating the prestack processing (Table 2) steps 3–7 in detail: (a) plotted as raw data, (b) with AGC (window length 250 ms) applied, (c) with additionally spectral balancing (whitened frequencies 10–100 Hz in slots of 5 Hz) applied, and (d) after an additionally velocity fan filter applied in the f-k domain (>550 m/s accepted). The red line denotes the 60 m source-receiver distance (offset) for near-offset preprocessing, the blue and red dashed lines denote the stretch mutes of 100% and 30% respectively, assigned during NMO correction. (e) shows the power spectrum for the processing steps A-D and (f) the f-k spectrum of processing step B with the f-k filtered (rejected) area for the processing step D (hashed-area). Green arrows mark high-frequency noise of source signal distortions that are amplified by AGC, blue/purple arrows point to reflections.

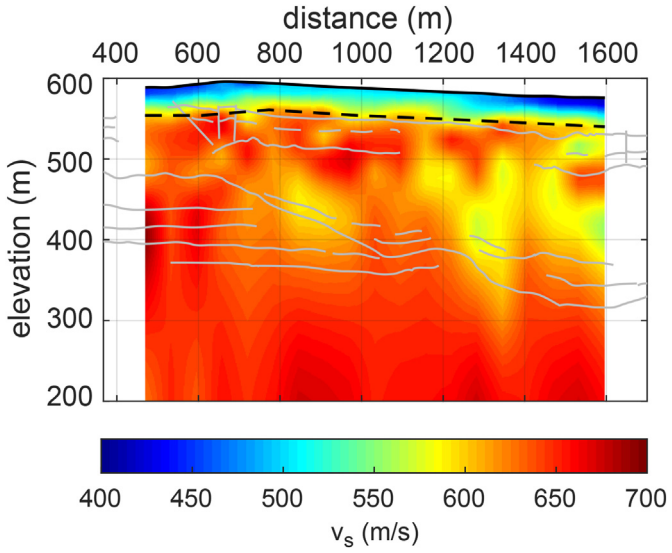

Fig. 5. Interval velocity in depth distribution, derived by the smoothed gradient method from the RMS stacking velocity field. The black dashed line divides the two areas described in the text. Main structures interpreted in the P-wave section taken from Burschil et al. (2018) are superimposed by gray lines for orientation. The RMS stacking velocities were analyzed by an interactive velocity analysis combining semblance, CMP-offset supergathers, and constant velocity stacks.

4. Results

4.1. Processing towards specific imaging purposes

Four different strategies pursue the goals: to highlight small-scale structures (1), locate the origin and incidence of reflections in the seismograms (2), generate a coherent image for the interpretation of large-scale structures (3), and sequentially compare relative amplitudes in P-wave and S-wave images (4).

The seismic section for small-scale structures images the structure of the TB in detail. The basin base is observed between 450 m and 350 m elevation (red arrow in Fig. 6a), i.e. 130 m to 200 m below the ground surface. Short coherent reflectors show internal structures of the basin fines (green arrow and black box in Fig. 6a). The section also reveals the till layers (purple arrow in Fig. 6a) and very shallow reflections inside fluvial deposits just below the surface (blue arrow in Fig. 6a).

To focus on steep angles of incidence and reflection, we restricted the offset range to 60 m (red line in Fig. 4) and processed the section using the same parameters as in the strategy to highlight small-scale structures (1). The seismic section with offset restriction (Fig. 6b) reveals the main structural image as in the entire offset range section (Fig. 6a) except for minor variations. The very shallow part shows the same coherent reflectors (e.g. blue arrows in Figs. 6a, b). Below 560 m elevation, differences in the reflection pattern occur, e.g., the prominent reflectors are less resolved (purple arrows in Figs. 6a, b). S-wave first arrivals cross the 60 m offset mark at ~0.2 s (Fig. 4d). By restricting the offset, parts of earlier reflection hyperbolas (e.g. purple arrows in Fig. 4) are excluded from the stacking process. Significant differences in the imaging quality of the basin base are not obvious (red arrows in Fig. 6a, b), even if prominent parts of the basin base reflection occur outside the 60 m offset range (blue arrows in Fig. 4). In the data beyond 60 m offset and between first breaks and basin base reflection (Fig. 4d), no significant signal contributes to the overall seismic image (cf. Fig. 6a, b).

The processing for a large-scale structural interpretation omits spectral whitening but applies additionally an f-k filtering after CMP stacking that smooth the stacked section prior to the poststack migration. This procedure enhances the reflector coherency of basin base (red arrow in Fig. 6c) as well as the till layers (purple arrows in Fig. 6c). The reflectors appear smoother and of lower central frequency, compared to the small-scale processed section (red/purple arrows in Fig. 6a). The reflection pattern of the basin fines (green arrow in Fig. 6c) and other

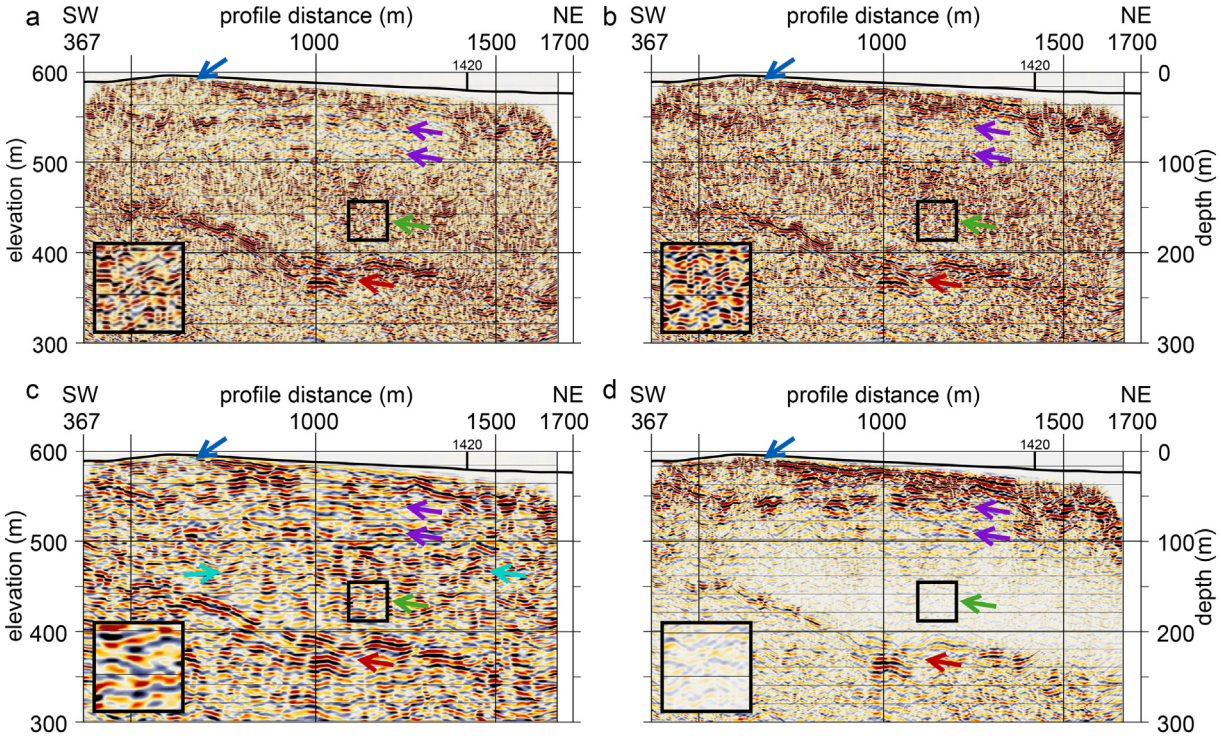

Fig. 6. S-wave sections according to different processing strategies of Table 2: The optimized processing for small-scale structures (a), near-offset restricted processing with maximum offset of 60 m (b), coherency enhanced image to highlight large-scale structures for interpretation (c), and processing with adapted amplitude scaling for comparison with P-waves (d). Zoom of the basin fines (black boxes). The arrows indicate the different reflection pattern discussed in the text.

Table 2
Processing steps for different processing strategies (see also the supplementary material for a flowchart of the different processing strategies).

		Processing strategy for			
		Highlighting small-scale structures (1)	Near-offset restricted processing (2)	Coherent imaging to interpret large-scale structures (3)	Comparing relative amplitude of P-wave and S-wave imaging (4)
Processing steps					
1	Geometry load	Applied			
2	Vertical stacking	Applied			
3	QC	Kill noisy traces			
4	Elevation static	Replacement velocity 300 m/s, final datum 600 m			
5	Offset restriction	All	<60 m	all	
6	Amplitude scaling	Automatic gain control (AGC), window length 250 ms			AGC, 1000 ms
7	Spectral whitening	10–100 Hz		Not applied	10–100 Hz
8	f-k-filtering	Fan filter >550 m/s accepted			
9	NMO-correction	Velocity distribution from interactive velocity analysis, 100% stretch mute			
10	Amplitude scaling	AGC, 250 ms			not applied
11	Residual statics	Correlation autostatics			
12	CMP-stacking	Mean summing, shift to final datum			
13	f-k-filtering	Not applied		fan filter < 0.7 ms/tr accepted	not applied
14	Time-migration	Implicit finite difference, angle 45 deg			
15	Data enhancement	Dip scan stack, aperture 7, −1-1 ms/tr			
16	Time-to-depth conversion	Smoothed stacking velocity distribution			

coherent patterns (cyan arrows in Fig. 6c) show low frequency horizontal reflectors, which are not obvious in the small-scale processed section (green arrow in Fig. 6a). Shallow reflections are imaged as well, but their structural information is less clear compared to the small-scale processed section (blue arrows in Figs. 6a, c).

To enable a structural comparison of P-waves and S-waves, it is required to process the data with a comparable amplitude scaling in depth. Major imaged structures are now the basin base reflector (red arrow in Fig. 6d) and the reflectors of the till layers and sequences (purple arrows in Fig. 6d). Shallow structures are still visible, as for the smaller AGC window (blue arrows in Figs. 6a, d). The internal structure of the basin fines is not visible anymore due to low amplitudes (green arrow in Fig. 6d). The adjusted scaling is therefore important: either to highlight small-scale structures or to structurally compare the seismic section with P-wave data.

4.2. Comparison of P-wave and S-wave imaging

The P-wave imaging (Burschil et al., 2018) reveals the sedimentary succession of the TB in detail as coherent reflectors (Fig. 7a). The interpretation is based on a seismic facies analysis aided by a cored research borehole and is described in Burschil et al. (2018). In summary, it shows molasse units below the basin base as well as the basin fill, from bottom to top: allochthon molasse, basal till, basin fines, till layers and sequences, and uppermost gravel/coarse sand. All S-wave sections, processed with different strategies, image the same overall structures (Fig. 6), especially in the large-scale version (Fig. 6c). The relative amplitudes in the P-wave and the S-wave sections show a comparable sequence (Fig. 7a vs. Fig. 6d). However, the benefit of the S-wave imaging becomes visible in the small-scale structure version. The shorter wavelength offers improved resolution and improved imaging of shallow depths up to 30 m below surface compared to the P-wave section (Fig. 7, box 1). In areas of conflicting dips or wedging units, S-waves resolve more structural details and lead to a different interpretation because the smooth reflectors of the P-wave section do not image the wedging of the till layer in detail (Fig. 7, box 2). The detailed vertical offset of reflectors enables the interpretation of faults (blue dashed line in Fig. 7, box 2). In addition, the P-wave section shows some significant areas of low amplitude response, which appear as transparent zones in the image, most likely caused by near-surface scattering (discussed in Burschil et al., 2018). This effect does not occur in the S-wave images, e.g. at the reflector of the basin base (Fig. 7, box 3). Furthermore, internal structures of the basin fines are resolved in the small-scale processing of the S-wave data.

5. Discussion

The different processing strategies comprise diverse processing steps and result in different seismic sections. Therefore, one has to keep in mind the applied processing steps when examining or interpreting the seismic sections.

A crucial part of the processing flow was the reduction of surface waves. Their stronger amplitudes compared to the reflections dominate during CMP-stacking and make recognition of reflections difficult. Several studies report a natural suppression of surface waves by very dry and compacted surfaces (Ghose et al., 2013) or by a paved surface layer (e.g. Inazaki, 2004; Krawczyk et al., 2013), as we observe for the asphalted ground condition of the profile (Fig. 3). Several tools are reported to reduce surface waves during processing by applying, e.g. a 45 Hz low-cut filter (Pugin et al., 2013), an unspecified dip filter (Carvalho et al., 2016), or f-k filtering (Beilecke et al., 2016; Polom et al., 2010, 2018). Schmelzbach et al. (2007) used a different approach to reduce linear onsets of Rayleigh surface waves, since f-k-filtering led to artefacts of the spatially irregular sampled data. They modeled Rayleigh surface waves in the τ-p domain and subtracted the synthetic signals from the original data in the time domain. The adaption of this approach did not succeed on real horizontally-polarized S-wave data (Van Zanen, 2004). For our data, this subtraction approach was not successful as well, probably due to the differences between Love and Rayleigh surface waves. Finally, f-k-filtering led to the best results for our (regularly sampled) data. Since an selective application led to artefacts, we applied this filter on all shot gathers over the entire profile, even if surface waves are not obvious in data recorded on consolidated ground (Fig. 4f).

Beside surface waves, the applied f-k filer also removed portions of direct and refracted S-wave events. Top muting by NMO stretch mute ensured that the final section does not contain stacked direct and refracted S-waves. We also tested a manually picked top mute, but it decreased the upper detection limit for shallow reflections significantly. However, a change of shallow seismic reflection signature coincides with the transition of the ground condition from asphalt road to gravel road, and, thus, could be related to stacked S-waves first arrivals. By carefully reviewing the shot gathers and considering all available data, we address this change to the geological structure on top of the terminal moraine of the LGM.

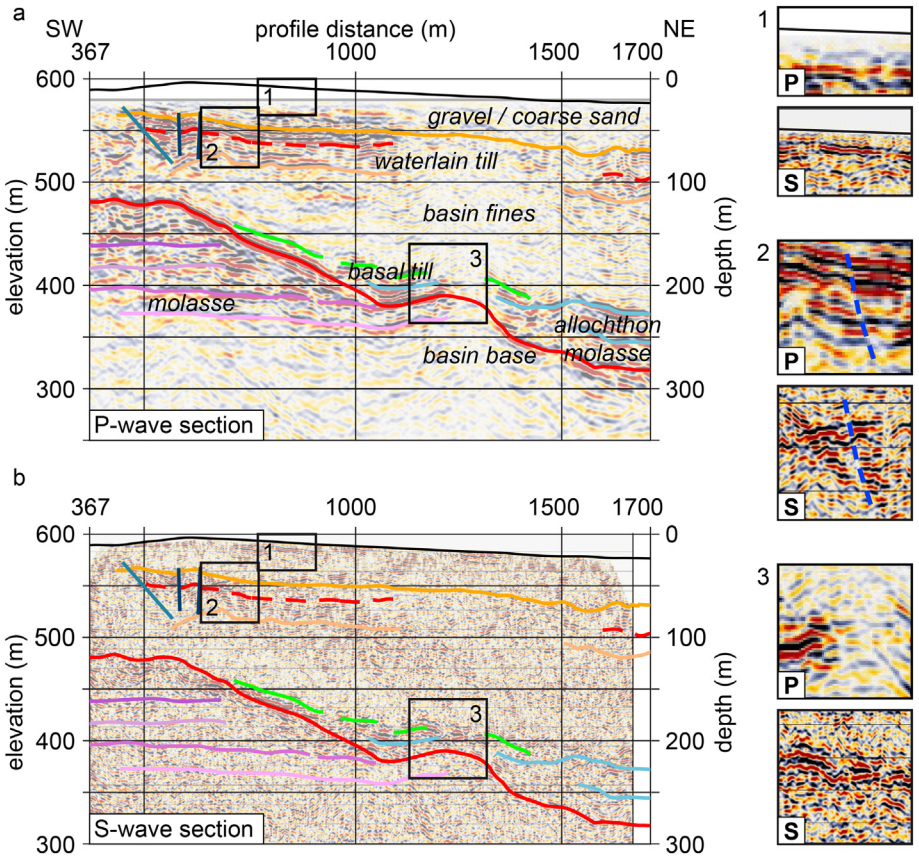

Fig. 7. P-wave seismic section from Burschil et al. (2018) (a) and S-wave depth sections (same as Fig. 6a with 50% transparency) (b), with the P-wave structural interpretation from Burschil et al. (2018) superimposed. Boxes 1–3 zoom in the P-wave and S-wave depth sections highlight shallow reflections (1), areas of improved resolution (2), and an apparently transparent P-wave region of low amplitude response (3). The blue dashed line in boxes 2 indicates a fault.

Amplitude scaling is a major issue in seismic processing. The majority of studies that uses S-waves skip true amplitude recovery for different purposes. Krawczyk et al. (2012) applied AGC scaling, because the high noise level in an urban setting impedes a statistically-based surface consistent processing. Brodic et al. (2018) scaled the amplitudes first using spherical divergence correction, but also applied AGC after NMO correction. Pugin et al. (2013) reported amplitude scaling by trace amplitude normalization, but applied AGC of a 1 s window prior to correlation. Ghose et al. (2013) and Carvalho et al. (2016) applied an unspecified gain correction. Beilecke et al. (2016) scaled using spherical divergence and subsequent trace normalization. In our case, true amplitude recovery was not successful, probably due to highly spatial-varying near-surface velocity variations and high amplitudes of source-generated noise. We decided to apply AGC for scaling, since it led to most applicable results. However, if P-wave and S-wave seismic sections are to be compared, one has to take the amplitude scaling into account. For the TB, the basin reflections are at ~0.2 s for P-waves and ~0.6 s for S-waves. The P-wave interval velocity is approximately three times higher than the S-wave velocity. To compare the relative sequential amplitudes of reflections, we set the AGC window to 1.0 s with respect to a 0.3 s AGC window length for the corresponding P-wave processing.

Elevation static correction served the changing topography along the profile. Considering near-surface velocity anomalies that we assume to be present in static corrections, was not possible, since we could not identify first arrival times of S-waves clearly due to interference with P-waves. This is probably the reason, why we do not detect the anomalies in a previous tomography study. However, Pugin et al. (2013) state that near-surface S-wave velocities are more homogenous than P-wave velocities, so that static corrections are not necessary. This is true considering the groundwater boundary, when the P-wave velocity often increase by more than a factor of two. It contrasts with the older work of Edelmann et al. (1983). They found S-wave statics to be 6 times larger than P-wave statics on their profile and argue that the groundwater table tends to equalize P-wave static corrections and does not influence S-wave propagation. Beilecke et al. (2016) required refraction static correction, since the overburden over karstic limestone shows a significant velocity increase along the limestone topography. Carvahlo et al. (2016) reports the successful application of residual static. In the case of our data, the application of residual static corrections did improved the coherency of the reflection signals.

A seismic processing with NMO correction and CMP stacking worked quite well for our site, as for other studies (e.g. Inazaki, 2004; Pugin et al., 2013; Wadas et al., 2016). Neither dip moveout correction nor prestack time migration improved the imaging quality of our data, as reported for study sites with conflicting and crosscutting dips (Carvalho et al., 2016; Beilecke et al., 2016). A test of prestack depth migration (PSDM), which we successfully applied on the P-wave data in this area, failed as well, probably because the offsets used for the tomographic inversion step are considerably smaller than those used in the P-wave data. Since we did not observe conflicting dips in our data and NMO correction with CMP stacking worked satisfactorily, a poststack migration seemed to be adequate.

The processing strategy for interpretation of large-scale structures generates an image of coherent reflections. Since we cannot trace all reflection segments back to the individual shot gathers, the seismic section may contain artefacts that are amplified by the smoothing effect of the second applied f-k filter. To avoid any geological interpretation of artefacts, we recommend to consider the seismic sections of other strategies as well for the final interpretation. Nonetheless, geological

large-scale structures produced by this strategy are better interpretable in the seismic images.

We calculate a vertical resolution (VR) for our study, on base of an average velocity in the range of 500 m/s and a dominant frequency around 70 Hz, to be ~1.75 m using the quarter wavelength criterion. However, our shallow reflections show wavelengths as short as 4 m, which corresponds to a VR of ~1 m. This is comparable to the VR reported in other studies. Krawczyk et al. (2012) calculates the VR to be 0.5 m theoretically, but estimates VR to be ~1 m due to other effects. Beilecke et al. (2016) state that VR was ~2 m for their survey, caused by the higher S-wave velocity of ~1100 m/s. Pugin et al. (2013) report a wavelength of 1.2 m to 3 m, which corresponds to a VR of 0.3 m to 0.75 m, based on the quarter wavelength criterion. This is approximately half the wavelength estimated for the corresponding P-wave data of 2–3.5 m maximum VR (Burschil et al., 2018), and, thus, S-waves provide a higher VR resolution than P-waves.

Between distances 1320 m and 1340 m in the profile, the surface waves show a significant lower velocity in an approximately 20 m wide region (Fig. 3). The origin for these anomaly that indicate a shallow low velocity anomaly, remains unclear. A pipeline from the pumping station to an elevated water tank (*PW* and *Wbh* in Fig. 1b, respectively) crosses the profile in that area. Nonetheless, the dimension of the affected region argues for a geological structure in the fluvial deposits of the outwash plain. A change of the seismic facies at shallow depth indicates a geological origin as well (cf. Fig. 6).

S-wave reflection imaging using near-offset data only produces a seismic section with a similar structural information for the entire offset range and it motivated us to conduct a 3-D S-wave survey (Burschil et al., 2019). In addition, near-offset S-wave acquisition also reduces costs compared to P-wave acquisition with a layout for the use of the "optimum window". This is supported by the costs of acquisition in terms of duration and man-power (Table 1). The operation progress of profile meters per day per person is higher for the S-wave survey than for the P-wave surveys for all profiles (117 m/day for S-wave and 99/day for P-wave) and for TB-1 in particular (162 m/day for S-wave and 96 m/day for P-wave). However, to assess precise costs for P-wave and S-wave seismic reflection imaging, other acquisition parameters have to be considered as well, since we used planted geophones for P-wave acquisition and landstreamer technique for S-wave application. However, the use of landstreamers is more feasible for short offset of S-wave recording. Furthermore, S-wave operation can be optimized by using only near-offsets, which we demonstrate to be sufficient for S-wave imaging.

6. Conclusions

Processing strategies of S-wave reflection data need to be adapted for the specific requirements of seismic imaging and interpretation purposes. Tailored processing strategies serve this issue and lead to seismic images for specific interpretations. For an improved resolution compared to P-waves, processing enhancing small-scale features with short window automatic gain control is able to unfold the significant advantages of S-waves. For interpretation of large-scale structures, we recommend the post-stack application of spatial filters to improve the coherency of reflectors. This strategy is a good choice, if structural interpretation based on P-wave data are not available. Adapted amplitude scaling during processing supports a classification of the reflection sequences for interpretation: display reflection strength vs. emphasize internal small-scale structures.

P-wave reflection seismic imaging is a robust method for near-surface imaging. S-waves complement P-wave imaging by contributing shallower reflectors, improved resolution, and structure imaging, where P-wave imaging fails. The parallel application of both methods is mutually beneficial and, thus, it is our favorable choice. However, using the adequate processing strategy, S-wave imaging is a cost-efficient alternative to high-resolution P-wave reflection imaging, since relatively small offsets produce highly-resolved images. Most information in the S-wave records was found within small offsets <60 m for an imaging depth up to 250 m, after we reduced surface waves by f-k-filtering. In the TB, acquisition costs of S-wave surveying were lower than for P-wave acquisition and could be reduced further by limiting the maximum offset. Nonetheless, S-wave imaging is highly site specific but it is an alternative to P-waves, at least for the presented site.

Author's statement

Both authors have same contribution to the work. They cooperated in seismic processing of S-wave data and wrote the manuscript together.

Declaration of Competing Interest

The authors declare that they have no known competing financial interests or personal relationships that could have appeared to influence the work reported in this paper.

Acknowledgement

The project was funded by German Research Foundation DFG, grants KR2073/3-1, GA749/5-1, BU2467/1-2. We thank Dr. Ulrich Polom and Dr. David C. Tanner for discussion and internal review the manuscript. Furthermore, we acknowledge the Co-editor-in-Chief Professor Jianghai Xia and the two anonymous reviewers for their helpful suggestions to improve the manuscript.

Appendix A. Supplementary data

Supplementary data to this article can be found online at https://doi.org/10.1016/j.jappgeo.2019.103927.

References

Beilecke, T., Krawczyk, C.M., Ziesch, J., Tanner, D.C., 2016. Near-surface fault detection using high-resolution shear wave reflection seismics at the CO2CRC Otway Project site, Australia. J. Geophys. Res. Solid Earth 121 (9), 6510–6532.

Bradford, J.H., Liberty, L.M., Lyle, M.W., Clement, W.P., Hess, S., 2006. Imaging complex structure in shallow seismic-reflection data using prestack depth migration. Geophysics 71 (6), B175–B181.

Brodic, B., Malehmir, A., Pugin, A., Maries, G., 2018. Three-component seismic land streamer study of an esker architecture through S-and surface-wave imaging. Geophysics 83 (6), B339–B353.

Buness, H., 2007. Improving the processing of vibroseis data for very shallow high-resolution measurements. Near Surface Geophys. 5 (3), 173–182.

Burschil, T., Beilecke, T., Krawczyk, C.M., 2015. Finite-difference modelling to evaluate seismic P-wave and shear-wave field data. Solid Earth 6 (1), 33–47.

Burschil, T., Buness, H., Tanner, D.C., Wielandt-Schuster, U., Ellwanger, D., Gabriel, G., 2018. High-resolution reflection seismics reveal the structure and the evolution of the Quaternary glacial Tannwald Basin. Near Surface Geophys. 16 (6), 593–610.

Burschil, T., Buness, H., Tanner, D., Gabriel, G., 2019. Seismic Imaging of Glacial Overdeepened Valleys using P- and S-waves. Proceedings of the 32nd Symposium on the Application of Geophysics to Engineering and Environmental Problems (SAGEEP), Portland, Oregon March 17–21.

Carvalho, J., Ghose, R., Alves, D., Leote, J., 2016. Earthquake-faulting-related deformation in soil evidenced in S-wave shallow reflection data: Field results from Portugal. Geophysics 81 (5), IM97–IM108.

Edelmann, H.A.K., Wiest, B., Schmoll, J., Keppner, G., 1983. The Data Processing. Prakla-Seismos Report 3+4/83, 26–37. Prakla-Seismos, Hannover.

Ellwanger, D., Wielandt-Schuster, U., Franz, M., Simon, T., 2011. The Quaternary of the southwest German Alpine Foreland (Bodensee-Oberschwaben, Baden-Württemberg, Southwest Germany). Q. Sci. J. 60 (2–3), 306–328.

Ghose, R., Carvalho, J., Loureiro, A., 2013. Signature of fault zone deformation in near-surface soil visible in shear wave seismic reflections. Geophys. Res. Lett. 40 (6), 1074–1078.

Hunter, J.A., Pullan, S.E., Burns, R.A., Gagne, R.M., Good, R.L., 1984. Shallow seismic reflection mapping of the overburden-bedrock interface with the engineering seismograph—some simple techniques. Geophysics 49 (8), 1381–1385.

Inazaki, T., 2004. High-resolution seismic reflection surveying at paved areas using an S-wave type land streamer. Explor. Geophys. 35 (1), 1–6.

Krawczyk, C.M., Polom, U., Trabs, S., Dahm, T., 2012. Sinkholes in the city of Hamburg—new urban shear-wave reflection seismic system enables high-resolution imaging of subrosion structures. J. Appl. Geophys. 78, 133–143.

Krawczyk, C.M., Polom, U., Beilecke, T., 2013. Shear-wave reflection seismics as a valuable tool for near-surface urban applications. Lead. Edge 32 (3), 256–263.
Malehmir, A., Lindén, M., Friberg, O., Brodic, B., Möller, H., Svensson, M., 2018. Unravelling contaminant pathways through a detailed seismic investigation, Varberg-Southwest Sweden. 24th European Meeting of Environmental and Engineering Geophysics.
Mavko, G., Mukerji, T., Dvorkin, J., 2009. The Rock Physics Handbook: Tools for Seismic Analysis of Porous Media. Cambridge University Press.
Pfiffner, O.A., 1986. Evolution of the north Alpine foreland basin in the Central Alps. Foreland Basins 219–228.
Polom, U., Hansen, L., Sauvin, G., L'Heureux, J.S., Lecomte, I., Krawczyk, C.M., Vanneste, M., Holliger, K., 2010. High-resolution SH-wave seismic reflection for characterization of onshore ground conditions in the Trondheim harbor, central Norway. Advances in Near-Surface Seismology and Ground-Penetrating Radar. SEG, Tulsa, pp. 297–312.
Polom, U., Rønning, J.S., Tassis, G., Gellein, J., Druivenga, G., 2017. Building site investigation by joint shear wave reflection seismic and geotechnical drilling at Tønsberg hospital area, eastern Norway. First Break 35 (8), 63–72.
Polom, U., Alrshdan, H., Al-Halbouni, D., Holohan, E.P., Dahm, T., Sawarieh, A., Atallah, M.Y., Krawczyk, C.M., 2018. Shear wave reflection seismic yields subsurface dissolution and subrosion patterns: application to the Ghor Al-Haditha sinkhole site, Dead Sea, Jordan. Solid Earth 9, 1079–1098.
Pugin, A.J.M., Pullan, S.E., Hunter, J.A., 2009. Multicomponent high-resolution seismic reflection profiling. Lead. Edge 28 (10), 1248–1261.
Pugin, A.J.M., Pullan, S.E., Hunter, J.A., 2013. Shear-wave high-resolution seismic reflection in Ottawa and Quebec City, Canada. Lead. Edge 32 (3), 250–255.
Schmelzbach, C., Horstmeyer, H., Juhlin, C., 2007. Shallow 3D seismic-reflection imaging of fracture zones in crystalline rock. Geophysics 72 (6), B149–B160.
Seguinot, J., Ivy-Ochs, S., Jouvet, G., Huss, M., Funk, M., Preusser, F., 2018. Modelling last glacial cycle ice dynamics in the Alps. Cryosphere 12 (10), 3265–3285.
Sheriff, R.E., Geldart, L.P., 1995. Exploration Seismology. Cambridge University Press.
Steeples, D.W., Miller, R.D., 1988. Seismic reflection methods applied to engineering, environmental, and ground-water problems. *Symposium on the Application of Geophysics to Engineering and Environmental Problems* 1988. Society of Exploration Geophysicists, pp. 409–461.
Steeples, D.W., Miller, R.D., 1998. Avoiding pitfalls in shallow seismic reflection surveys. Geophysics 63 (4), 1213–1224.
Tschache, S., Wadas, S.H., Polom, U., Krawczyk, C.M., 2018. Combination of 2D shear wave reflection seismics and travel time analysis of borehole geophone data for the investigation of a Sinkhole area. The Sinkhole Conference 2018. https://doi.org/10.5038/9780991000982.1019.
Uhlemann, S., Hagedorn, S., Dashwood, B., Maurer, H., Gunn, D., Dijkstra, T., Chambers, J., 2016. Landslide characterization using P-and S-wave seismic refraction tomography—The importance of elastic moduli. J. Appl. Geophys. 134, 64–76.
Van Zanen, L.F., 2004. Removing Love Waves from Shallow Seismic SH-Wave Data. Doctoral thesis, TU Delft. http://resolver.tudelft.nl/uuid:d467c131-3e61-47b1-809a-3b15f69b7765.
Wadas, S.H., Polom, U., Krawczyk, C.M., 2016. High-resolution shear-wave seismic reflection as a tool to image near-surface subrosion structures-a case study in Bad Frankenhausen, Germany. Solid Earth 7 (5), 1491.
Wadas, S.H., Tanner, D.C., Polom, U., Krawczyk, C.M., 2017. Structural analysis of S-wave seismics around an urban sinkhole: evidence of enhanced dissolution in a strike-slip fault zone. Nat. Hazards Earth Syst. Sci. 17 (12), 2335.
Winsemann, J., Lang, J., Polom, U., Loewer, M., Igel, J., Pollok, L., Brandes, C., 2018. Ice-marginal forced regressive deltas in glacial lake basins: geomorphology, facies variability and large-scale depositional architecture. Boreas 47 (4), 973–1002.